REAL-TIME CORRECTIONS FOR A LOW-COST HYPERSPECTRAL INSTRUMENT

M. B. Henriksen, J. L. Garrett, E. F. Prentice, A. Stahl and T. A. Johansen

Center for Autonomous Marine Operations and Systems (AMOS)
Department of Engineering Cybernetics
Norwegian University of Science and Technology
O.S. Bragstads plass 2D, 7034 Trondheim, Norway

F. Sigernes

University Centre in Svalbard (UNIS)
N-9171 Longyearbyen, Norway

ABSTRACT

The development of a hyperspectral imager (HSI) made from commercial off-the-shelf (COTS) parts enables the use of hyperspectral imaging on smaller low-cost platforms such as cubesats, drones, or other autonomous vehicles. However, HSIs built from COTS parts often suffer from more pronounced optical distortions, such as 'smile' and 'keystone', due to the shifted balance between cost and image quality. In this proceeding, radiometric, spectral, and geometric calibrations of a COTS HSI are presented. Furthermore, the calibrations are used to develop a real-time software-based spectrogram correction. The corrections will enhance the capability of small, autonomous platforms in using hyperspectral imaging.

Index Terms— Hyperspectral imager, COTS, Calibration, Smile, Keystone

1. INTRODUCTION

Hyperspectral imagers (HSIs) reveal the characteristic spectra of different objects in a scene, which allows for accurate classification and analysis. However, most HSIs are large enough to make operation from a drone difficult, which limits their use in surveying and conservation. One HSI developed for drone applications is the HSI V4, which is based on a push-broom design [1, 2]. It is built using commercial off-the-shelf (COTS) components and 3D-printed parts. It is designed to be cheap, easy to assemble and simple to replicate. With its small mass of less than 200 g, it can be easily integrated in existing autonomous systems. The specifications of the imager are shown in Table 1, and an optical diagram is depicted in Figure 1. The spectral range is limited by an anti-reflection coating that blocks light below 400 nm and second order effects that appear above 800 nm.

Table 1: Specifications of the HSI V4.

Parameter	**Specification**
Camera head	iDS UI-3360CP-NIR-GL R2
Image size	(1088, 2048) pixels
Spectral range	400 - 800 nm
FWHM	1.4 nm
Grating	600 grooves/mm, transmission
Slit height	3 mm
Slit width	25 μm

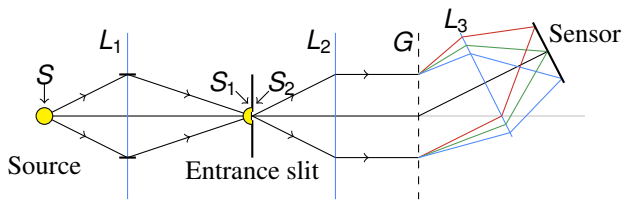

Fig. 1: Optical diagram of the HSI V4. S is area of the light source, S_1 the area of the source image, and S_2 area of the entrance slit. L_1, L_2 and L_3 are the lenses in the system, and G the transmission grating.

There are, however, trade-offs inherent to the simplified design. 3D-printed components can cause alignment issues and COTS components may introduce greater optical distortions in the system. While these unwanted effects are expected, it is important to calibrate and correct for them be-

The Research Council of Norway is acknowledged for funding to AMOS (grant number 223254) and MASSIVE (grant number 270959). JLG also acknowledges that this work was carried out during the tenure of an ERCIM 'Alain Bensoussan' Fellowship Programme.

fore the data can be relied on. Since the HSI is planned to be used with on-board data processing and image analysis in drones and satellites, real-time correction of the captured data is critical.

A typical spectral misregistration is smile [3], which is a change in the central wavelength in a spectral channel as a function of the slit height. A typical spatial misregistration is keystone, which is a change in the position of the same spatial pixel in the scene as a function of wavelength. These effects distort the spectral signatures of targeted objects and can reduce the detection and classification accuracy [4].

In this proceeding, the smile and keystone effects are characterized and corrected. Spectral and radiometric calibration are performed. The computation time of corrections derived from the calibrations applied to HSI spectrograms is shown to be low enough to achieve real-time processing.

2. METHODS

The framework that is used to apply corrections to the spectrograms, including calibration, is first presented. Then, the procedures for spectral and radiometric calibration are described, followed by a method for detecting smile and keystone effects.

2.1. Framework for applying corrections

Because there are many comprehensive and fast linear algebra software packages, the corrections are formulated as a matrix operation. The raw spectrogram is written as a 1-D vector, U (N spectral bands, M spatial pixels, NM total pixels). A matrix $\mathbf{H} \equiv \mathbf{H}_{\text{ks}}\mathbf{H}_{\text{rad}}$ is defined to correct the spectrogram

$$V = \mathbf{H}U, \tag{1}$$

where V is the corrected spectrogram, $\mathbf{H}_{\text{ks}}$ is the keystone and smile correction, and $\mathbf{H}_{\text{rad}}$ is the radiometric correction. The goal of the calibration below is to determine the matrices $\mathbf{H}_{\text{ks}}$ and $\mathbf{H}_{\text{rad}}$. The matrix $\mathbf{H}$ only needs to be determined once to correct many frames.

Because $\mathbf{H}$ is large ($(NM)^2 \approx 10^{12}$ elements), sparse matrices are used to ease computation and data storage, which is possible because most of the elements are zero [5]. The corrections are implemented in SciPy [6].

2.2. Wavelength calibration

Wavelength calibration determines the relationship between wavelength and pixel position along the horizontal axis of the spectrogram. The wavelength pixel relation is approximately

$$\lambda \approx a_0 + a_1 \cdot p_\lambda + a_2 \cdot p_\lambda^2, \tag{2}$$

where λ is the wavelength and p_λ the spectral pixel index [7].

For the wavelength calibration, argon and mercury-argon wavelength calibration lamps (Newport Models 6030 and 6035, respectively) are used together with a Newport 6044 AC power supply to provide calibration wavelengths from about 400 to 900 nm. A 30 cm integrating sphere (Model ISS-30-VA, Gigahertz Optik), with 10 cm output, is used for uniform illumination. The imager is mounted in front of the sphere, and the calibration lamp is placed in the inlet. The calibration lamp is switched on while all other light is off, and a test image is taken. The settings are adjusted so that the highest peaks are nearly overexposed, to maximize the signal.

The wavelength calibration coefficients are calculated by identifying the known reference peaks of argon and mercury with the observed peaks.

2.3. Radiometric calibration

The goal of radiometric calibration is to correctly convert the raw data from sensor count to spectral radiance so that the measurements are comparable to data from other instruments. As radiometric calibration relies on the wavelength calibration [8], the wavelength calibration must be performed first.

The calibration factor for each pixel, or ratio between absolute units and counts, is given as

$$K = \frac{L}{C} \quad \Big[\frac{\text{mW}}{\text{m}^2 \text{ sr nm counts}}\Big], \tag{3}$$

where L is the radiance, depending on wavelength, in absolute units and C is the background corrected sensor counts of the radiometric source [9].

For the radiometric calibration, the integrating sphere light source is used as the calibration light source. The imager is placed in front of the integrating sphere outlet to illuminate the full field of view. The settings are adjusted so that the spectrogram is not overexposed.

The radiometric calibration coefficients are then calculated using Equation (3) for every pixel in about 30 frames, and the average coefficient matrix, made by the average coefficient for each pixel, is further used.

The coefficients K in Equation (3) are placed along the diagonal of $\mathbf{H}_{\text{rad}}$. The ith diagonal element corresponds to the calibration coeficient of the ith pixel in the image. Portions of the spectrogram which receive light below the noise level are set to zero because they do not contribute any information. The off-diagonal elements of $\mathbf{H}_{\text{rad}}$ are also set to zero, because the calibration of each pixel is independent.

2.4. Smile and keystone characterization

A set-up is designed to detect smile and keystone in a small laboratory environment. A pattern is used in combination with spectral light sources to obtain intersection points in the spectrogram, which are then used to detect and correct smile and keystone in the imager. A Zeiss Makro-Planar 100 mm f/2 lens with Nikon mount is used as collimator lens. A 3D-printed striped pattern is placed behind the collimator lens so

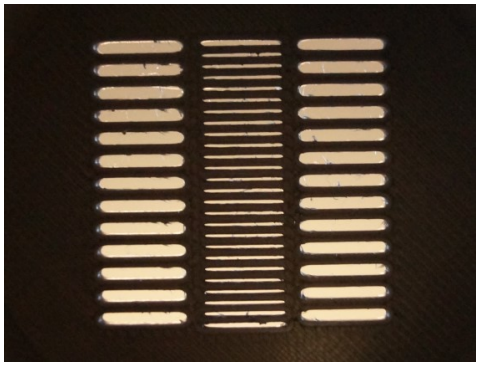

Fig. 2: The 3D printed pattern.

that it is in the HSI's focal plane. The striped pattern is shown in Figure 2.

The detection and correction of the smile and keystone effects is based on the method presented in [10]. This method allows smile and keystone to be corrected simultaneously, which is preferable as the effects depend on each other. The method is based on creating and finding known control points, called ground control points (GCPs) in the image, and then determining the smile and keystone effects using these points. The correction is performed by mapping the GCPs in the image to known reference points [11]. A second-order polynomial in the pixel indices (p_λ and p_y) is calculated from the GCPs in order to determine a pixel-by-pixel map from the raw spectrogram to a rectified spectrogram.

The distortion in the original image can be approximated by a two-dimensional quadratic polynomial distortion model

$$f_\eta(p_\lambda, p_y) = \sum_{l,k=0}^{l+k\leq 2} a_{\eta lk} p_\lambda^l p_y^k, \tag{4}$$

where p_λ and p_y are the pixel indices in the raw frame, the η subscript indicates either λ or y, f_λ and f_y identify a position in the corrected frame, and the $a_{\eta lk}$ are the calibration coefficients. The calibration coefficients are determined using the pseudo-inverse method and the positions of the GCPs in the raw and corrected frames [10, 11].

The matrix $\mathbf{H}_{\text{ks}}$ is calculated from the polynomial map. Because the pixels in the raw spectrogram are mapped to positions that may be in-between several pixels, the radiance is split between four pixels in the corrected spectrogram. Four pixels are used in order to fully correct for geometrical distortions while introducing minimal blur. The jth pixel in the raw spectrogram is represented by the jth column of $\mathbf{H}_{\text{ks}}$. The elements, H_{ij}, of the column take the values

$$H_{(r_\lambda, r_y)j} = (1-\Delta_\lambda)(1-\Delta_y), \tag{5a}$$
$$H_{(r_\lambda+1, r_y)j} = \Delta_\lambda(1-\Delta_y), \tag{5b}$$
$$H_{(r_\lambda, r_y+1)j} = (1-\Delta_\lambda)\Delta_y, \tag{5c}$$
$$H_{(r_\lambda+1, r_y+1)j} = \Delta_\lambda\Delta_y, \tag{5d}$$

where

$$r_\eta(p_\lambda, p_y) = \text{floor}(f_\eta(p_\lambda, p_y)), \tag{6}$$

and

$$\Delta_\eta(p_\lambda, p_y) = f_\eta(p_\lambda, p_y) - r_\eta(p_\lambda, p_y). \tag{7}$$

The other elements of the column are set to zero. Note that $\sum_i H_{ij} = 1$, so the total radiance is preserved.

Spectrograms with distinguishable ground control points are measured using the collimator lens and the striped pattern, together with argon and mercury spectral light sources. The HSI is placed in front of the lens looking into the center, as seen in Figure 3, to image the most narrow slits shown in Figure 2. The pattern is illuminated from behind by the spectral lamp, used together with the integrating sphere to ensure uniform illumination. At least 30 images are collected for each spectral lamp to minimize random noise by averaging.

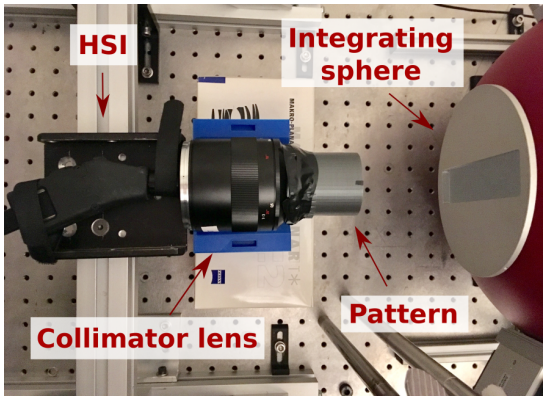

Fig. 3: The collimator set-up with the HSI V4 in the lab. The HSI V4 looks into the center of the collimator lens, and the whole set-up points towards the integrating sphere outlet.

The polynomial coefficients are calculated using all the spectrograms collected, and a randomly chosen spectrogram is used for measuring smile and keystone before and after correction. The smile effect is estimated from all of the GCPs found in each spectral line, while the keystone in the system is estimated by making a linear fit of the position of all the GCPs in each spatial line.

3. RESULTS

The results from spectral and radiometric calibration, as well as smile and keystone corrections, and the computation time for the full corrections are presented.

3.1. Calibration

Figure 4 shows the argon and mercury peaks used for spectral calibration, the measured radiance from radiometric calibration, and the reference spectrum from the integrating sphere.

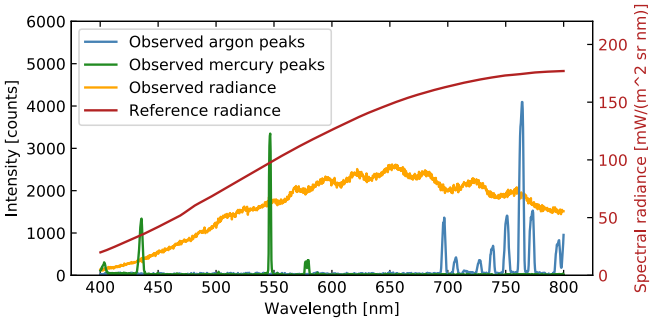

Fig. 4: The observed argon and mercury peaks from spectral calibration, the observed signal from the radiometric calibration (left), and the reference spectrum of the integrating sphere (right).

The observed data is measured in counts, while the reference data is used to convert from counts to spectral radiance.

3.2. Smile and keystone

The intersection points made by the striped pattern and the calibration lamps are shown in Figure 5. The curvature of the spectral lines is visible before correction in Figure 5a, indicating a high smile effect, while the keystone effect does not appear as extreme. The same frame after correction can be seen in Figure 5b, where the lines now appear straight, indicating less smile effect in the image.

The reduction of smile and keystone are also shown in Figure 6. Figure 6a shows that the shift due to smile after correction is centered around zero, and shows an overall improvement for the full range. The error due to keystone, (Figure 6b), shows improvement, but is not centered around zero. This could be due to inaccurate detection of the GCPs used in the distortion model. A narrower striped pattern may allow smaller GCPs which, in turn, may help improve the results.

3.3. Computation time

The computation time of the corrections is tested on a desktop computer (Intel i7-4790S, 3.20 GHz). The matrix $\mathbf{H}$ requires about 10 ms/frame or 2.5 ms/MB as each frame is roughly 4 MB in size. When broken up into its constituent parts, however, $\mathbf{H}_{\text{rad}}$ requires only 8 ms/frame, but $\mathbf{H}_{\text{ks}}$ requires 17 ms. The time required correlates with the density (proportion non-zero elements) of the matrices, which is 7.4×10^{-7}, 4.5×10^{-7}, and 1.8×10^{-6}, respectively. Once the calibrations are known, it takes about 30 s to generate $\mathbf{H}_{\text{ks}}$, 2 ms to generate $\mathbf{H}_{\text{rad}}$, and about 130 ms to generate $\mathbf{H}$ from its constituent matrices. Thus, generating $\mathbf{H}$ once and then re-using it is critical to the speed of the corrections.

The processing time is comparable in order of magnitude to the time reported in [12], in which complete radiometric and geometric corrections are achieved in 0.445 ms/MB (0.89 s for a 2 GB frame). The procedure in [12] is optimized for a field-programmable gate array (FPGA) with a digital signal processor and it is focused on geo-referencing rather than calibration. Real-time calibration has also been demonstrated by [13] for airborne hyperspectral imagery campaigns correcting for spectral shifts, keystone, and smile. Comparing the results to these other experiments suggests that it is possible to integrate the corrections into a more comprehensive data processing pipeline.

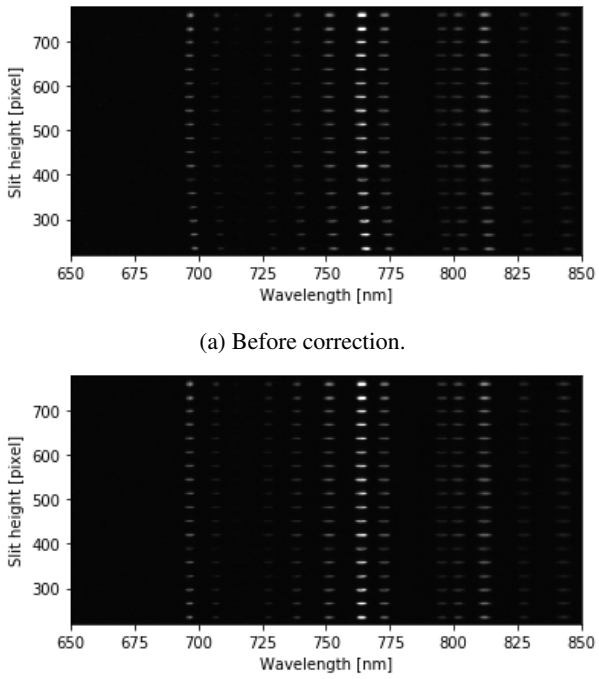

(a) Before correction.

(b) After correction.

Fig. 5: Chosen area of frame used for smile and keystone detection, showing the GCPs created by the pattern and the argon spectral lamp before and after correction.

4. CONCLUSIONS

Above, it is shown that although COTS hyperspectral imagers suffer significant misregistration effects, it is possible to mitigate these errors in real time through careful characterization and calibration. Spectral and radiometric calibrations are used to determine the radiance that the camera observes. The smile and keystone characterization is used to define a real-time correction that runs at a rate of about 10 ms/frame. The corrections are shown to improve the images, by reducing both the smile and keystone effect.

Although real-time processing speed is achieved, a more accurate smile and keystone characterization would improve the correction. Adapting the algorithm to work on pro-

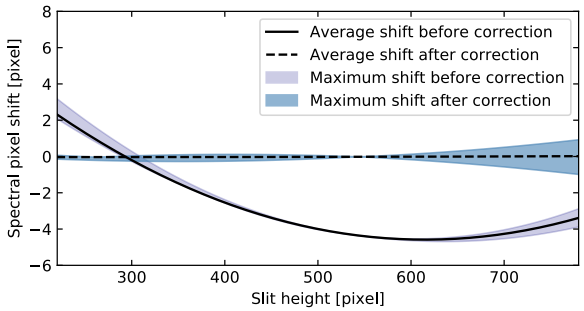

(a) Errors due to smile.

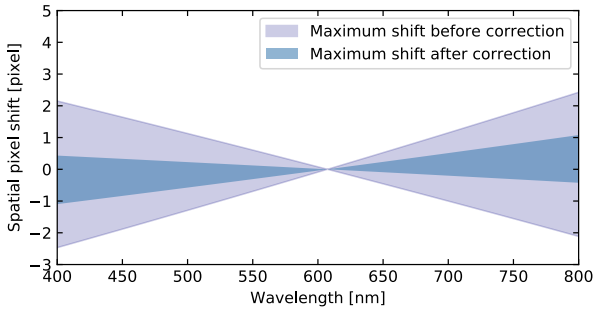

(b) Errors due to keystone.

Fig. 6: Reduction of smile and keystone errors in the HSI V4.

grammable logic or graphical processing units may improve its speed, and would aid in its integration with autonomous systems. Other effects such, as stray light, polarization sensitivity, and temperature dependency, could also be characterized, and corrections for these effects could be included in the final correction matrix.

5. REFERENCES

[1] F. Sigernes et al., "Do it yourself hyperspectral imager for handheld to airborne operations," *Optical Express*, vol. 26, pp. 6021–6035, 2018.

[2] J. Fortuna and T. A. Johansen, "A Lightweight Payload for Hyperspectral Remote Sensing Using Small UAVs," in *Proc. of the 9th Workshop on Hyperspectral Image and Signal Processing: Evolution in Remote Sensing*, 2018.

[3] A. Fridman, G. Høye, and T. Løke, "Resampling in hyperspectral cameras as an alternative to correcting keystone in hardware, with focus on benefits for optical design and data quality," *Optical Engineering*, vol. 53, no. 5, 2014.

[4] N. Yokoya, N. Miyamura, and A. Iwasaki, "Detection and correction of spectral and spatial misregistrations for hyperspectral data using phase correlation method," *Applied Optics*, vol. 49, no. 24, pp. 4568–4575, 2010.

[5] T. A. Davis, *Direct methods for sparse linear systems*, Society for Industrial and Applied Mathematics, 2006.

[6] Eric Jones, Travis Oliphant, Pearu Peterson, et al., "SciPy: Open source scientific tools for Python," 2001.

[7] F. Sigernes, "Basic Hyper Spectral Imaging," 2018, Lecture notes NTNU, Retrieved from `http://kho.unis.no/doc/TTK20/BASIC_HYPER_SPECTRAL_IMAGING.pdf`.

[8] X. Yu et al., "Laboratory Spectral Calibration and Radiometric Calibration of Hyper-spectral Imaging Spectrometer," in *ICSAI: 2nd International Conference on Systems and Informatics, ICSAI 2014*, 2015, pp. 871–875.

[9] F. Sigernes et al., "Absolute calibration of optical devices with a small field of view," *Journal of Optical Technology*, vol. 74, no. 10, pp. 669–674, 2007.

[10] K. C. Lawrence et al., "Calibration of a Pushbroom Hyperspectral Imaging System for Agricultural Inspection," *Transaction of the ASAE*, vol. 46, no. 2, pp. 513–521, 2003.

[11] R. A. Schowengerdt, *Remote Sensing: Models and Methods for Image Processing*, Elsevier Inc., 2007.

[12] B. Qi, H. Shi, Y. Zhuang, H. Chen, and L. Chen, "On-Board, Real-Time Preprocessing System for Optical Remote-Sensing Imagery," *Sensors (Basel)*, vol. 18(5), pp. 1328, 2018.

[13] S. Blaaberg, T. Løke, I. Baarstad, A. Fridman, and P. Koirala, "Hyspex odin-1024: a new high-resolution airborne hsi system," *Proc. SPIE 9070 Infrared Technology and Applications XL*, vol. 90700L, 2014.